Ultrafast Light-Induced Lifshitz Transition

Samuel Beaulieu[1]*, Shuo Dong[1], Nicolas Tancogne-Dejean[2]*, Maciej Dendzik[1,3], Tommaso Pincelli[1], Julian Maklar[1], R. Patrick Xian[1], Michael A. Sentef[2], Martin Wolf[1], Angel Rubio[2,4], Laurenz Rettig[1], and Ralph Ernstorfer[1]*

[1]*Fritz Haber Institute of the Max Planck Society, Faradayweg 4-6, 14195 Berlin, Germany.*

[2]*Max Planck Institute for the Structure and Dynamics of Matter, Luruper Chaussee 149, 22761 Hamburg, Germany.*

[3]*Department of Applied Physics, KTH Royal Institute of Technology, Electrum 229, SE-16440, Stockholm, Kista, Sweden.*

[4]*Center for Computational Quantum Physics (CCQ), The Flatiron Institute, 162 Fifth Avenue, New York NY 10010.*

Fermi surface is at the heart of our understanding of metals and strongly correlated many-body systems[1]. An abrupt change in the Fermi surface topology, also called Lifshitz transition[2], can lead to the emergence of fascinating phenomena like colossal magnetoresistance[3] and superconductivity[4,5]. While Lifshitz transitions have been demonstrated for a broad range of materials and using different types of static external perturbations such as strain[6,7], doping[4,5], pressure[3,8] and temperature[9,10], a non-equilibrium route toward ultrafast and transient modification of the Fermi surface topology has not been experimentally demonstrated. Combining time-resolved multidimensional photoemission spectroscopy[11] with state-of-the-art TDDFT+U simulations[12–14], we introduce a scheme for driving an ultrafast Lifshitz transition

in the correlated Weyl semimetal T_d-$MoTe_2$[15–18]. We demonstrate that this non-equilibrium topological electronic transition finds its microscopic origin in the dynamical modification of the effective electronic correlations. These results shed light on a novel ultrafast and all-optical scheme for controlling the Fermi surface topology in correlated quantum materials.

The free quantum electron gas approximation within the Drude-Sommerfeld model of metallic solids leads to purely parabolic band dispersion and spherical Fermi surfaces. However, electron-lattice and electron-electron interactions break the quadratic energy-momentum relationship, leading to complex electronic band dispersions and Fermi surface shape and topology. The Fermi surface, which separates unoccupied from occupied electronic states, is of paramount importance to understand a broad range of phenomena in metallic and semimetallic systems. To cite pioneering work of Kaganov and Lifshitz: "the Fermi surface is the stage on which the drama of the life of the electron is played out"[1].

Equilibrium tuning of macroscopic parameters such as temperature[9,10], pressure[3,8], strain[6,7] or doping[4,5], have all been demonstrated to be capable of modifying electronic band structures, which is, in some prominent cases, accompanied by an abrupt change in the Fermi surface topology, a phenomenon known as *Lifshitz transition*[2]. A Lifshitz transition is often concurrent with strong modifications of material properties since low-energy excitations, relevant to many electronic, magnetic, and optical properties, occur nearby the Fermi surface boundary. For example, in black phosphorus, the sudden modification of the Fermi surface topology induced by pressure has been shown to lead to the emergence of colossal positive magnetoresistance and of nonlinear

field dependence of Hall resistivity[3]. Moreover, it was demonstrated that Lifshitz transitions coincide with the onset of superconductivity in electron-doped iron arsenic superconductors[4], and that such electronic topological transition can enhance superconductivity in electron-doped monolayer FeSe[5]. While inducing Lifshitz transitions using equilibrium tuning methods is now well-established, a protocol for ultrafast Fermi surface topology engineering would be highly desirable since it would allow controlling materials properties on unprecedented timescales. However, until now, this goal remains elusive.

In this Article, we experimentally and theoretically demonstrate a novel route to induce a Lifshitz transition in correlated materials, based on photoexcitation using ultrashort laser pulses. We apply this scheme to the topological type-II Weyl semimetal T_d-$MoTe_2$, a material that is known to be in the vicinity of a Coulomb-interaction-induced Lifshitz Transition[19]. Experimentally, we directly map the dynamical evolution of its band structure and its Fermi surface on ultrafast timescales using state-of-the-art time-resolved multidimensional photoemission spectroscopy[11,20]. Theoretically, we investigate the microscopic origin of the non-equilibrium Lifshitz transition using extensive time-dependent self-consistent Hubbard U calculations (TDDFT+U)[12–14].

$\mathrm{T_d}$-$\mathrm{MoTe_2}$ belongs to the transition metal dichalcogenide (TMDC) family. TMDCs have recently attracted tremendous interest, mostly because of the unique combination of strong spin-orbit splitting, locally broken inversion symmetry, and enhanced electronic and mechanical properties, making them very interesting for fundamental studies as well as for applications in electronics, spintronics, optoelectronics, and twistronics. In particular, $\mathrm{MoTe_2}$ is known to undergo a struc-

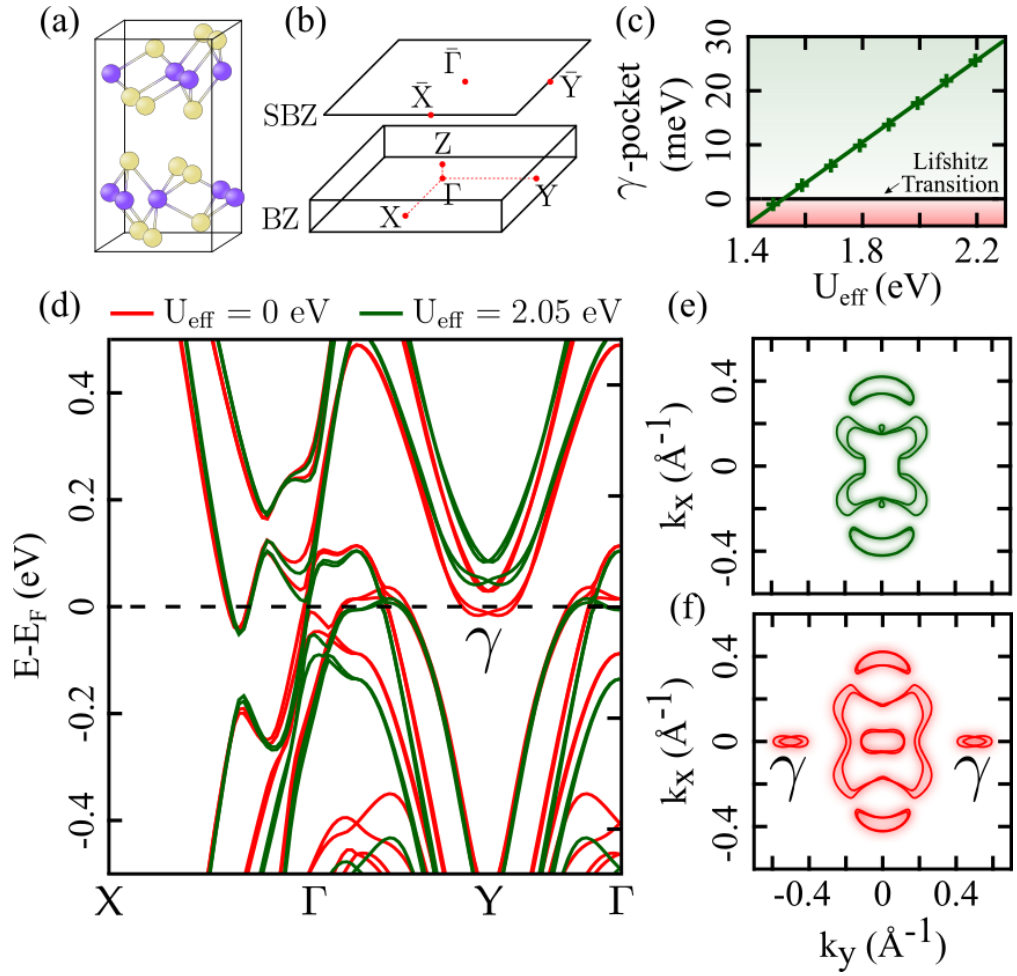

Figure 1: **Coulomb-interaction-induced Lifshitz transition in topological Weyl semimetal $\mathbf{T_d}$-$\mathbf{MoTe_2}$.** (a) A schematic of the crystal structure of the low-temperature orthorhombic $\mathrm{T_d}$-phase of $\mathrm{MoTe_2}$ and (b) its associated Brillouin zone (BZ) and surface Brillouin zone (SBZ). (c) The equilibrium phase diagram revealing the effect of the Hubbard $U_{\mathrm{eff}} = U - J$ (J being the Hund's exchange) on the position of the γ-pocket relative to the Fermi energy. The dots are data points obtained from DFT+U simulations whereas the thick line is a linear fit to the data, serving as a guide to the eye. (d) The electronic band structure of $\mathrm{T_d}$-$\mathrm{MoTe_2}$ for the equilibrium self-consistently calculated value of $\mathrm{U_{eff}}$ = 2.05 eV (in green) and for the reduced value of U_{eff} = 0 eV (below the adiabatic Lifshitz transition), and their respective Fermi surface cuts taken at k_z = 0, (e)-(f). In (f), one can clearly see the hallmark of the Coulomb-induced Lifshitz transition–the appearance of γ-electron pockets at the Fermi surface.

tural phase transition from the monoclinic and topologically trivial semimetallic (1T'-) phase to the orthorhombic type-II Weyl semimetallic (T_d-) phase, when cooled below $\sim$ 250 K (Fig. 1(a)-(b)). T_d-$MoTe_2$ has been shown to exhibit extremely large and unsaturated magnetoresistance[21], and emerges as a topological type-II Weyl semimetal[15–18], characterized by tilted Weyl cones originating from a protected crossing between the valence and conduction bands in reciprocal space[22]. Weyl points act as a topological charge, *i.e.* either a source or a sink of Berry curvature, leading to many fascinating physical phenomena, including the emergence of Fermi arcs[23,24] as well as various transport anomalies[25]. Elucidating the detailed electronic structure of this prominent 2D Weyl semimetal has been subject of a lot of experimental and theoretical efforts. Recently, combined static soft X-ray ARPES and DFT+U studies reported that the inclusion of corrected on-site Coulomb interaction (Hubbard U) is essential to reproduce the experimentally measured electronic band structure and Fermi surface of T_d-$MoTe_2$[19,26].

Fig. 1(d) shows the calculated band structures for different values of the effective Hubbard U_{eff}: in green for the self-consistent value (U_{eff} = 2.05 eV) obtained using our *ab initio* method[12], and in red, for a reduced U_{eff} = 0 eV. While the modification of the effective on-site Coulomb interaction leaves the band dispersions along Γ-X mostly unchanged, it leads to a significant energy shift of two slightly spin-orbit split electron pockets, located close to the Y high symmetry points. Fig. 1(c) shows the energy position of the lower-lying γ-pocket as a function of the effective Hubbard $U_{\rm eff}$. Around $U_{\rm eff} \sim$ 1.5 eV, the γ-pocket is crossing the Fermi level, leading to a Lifshitz transition, as evidenced by the Fermi surface cuts depicted on Fig. 1 (e)-(f), in good agreement with the predictions of Xu *et al.*[19]. Because T_d-$MoTe_2$ is in the vicinity of a Coulomb-induced

Lifshitz transition, it is an interesting candidate for investigating the possibility to control the Fermi surface topology on ultrafast timescale, using laser photoexcitation.

We used time-resolved multidimensional photoemission spectroscopy to characterize the non-equilibrium electronic structure of $\mathrm{T_d}$-$\mathrm{MoTe_2}$. Our experimental setup includes a monochromatized high-order harmonic generation (HHG)-based XUV source, at 500 kHz repetition rate and centered around 21.7 eV (bandwidth: 110 meV FWHM, pulse duration: $\sim$20 fs FWHM)[27], spanning the full extent of the surface Brillouin zone in parallel momentum. Both IR-pump (1030 nm, 140 fs FWHM, 6.7x10^9 $\mathrm{W/cm^2}$) and XUV-probe are p-polarized and focused onto the $\mathrm{T_d}$-$\mathrm{MoTe_2}$ sample, handled and cooled to 30 K by a 6-axis cryogenic manipulator. The photoemitted electrons are collected by a time-of-flight momentum microscope[20], a multidimensional detection scheme to obtain the four-dimensional (E_B,k_x,k_y,t) non-equilibrium electronic structure (see Fig. 2(a)-(b))[11]. More information about the experimental setup can be found in Methods.

We tracked the evolution of the Fermi surface as a function of pump-probe delay (Fig. 2 (c)-(g)). After the interaction with the femtosecond IR pump pulse, the appearance of the γ-pockets is visible (Fig. 2(d)) on the Fermi surface. This is the hallmark of the laser-driven Lifshitz transition. At longer delays, the signal in the γ-pockets at the Fermi energy continues to increase (Fig. 2(e)), followed by a gradual decays (Fig. 2(f)), and eventually vanish after $<$ 1 ps (Fig. 2(g)), indicating the recovery of the equilibrium Fermi surface topology.

The multidimensional photoemission data allow us to gain an additional perspective on the laser-induced dynamics by looking at the energy-resolved differential signal along Y-Γ-Y ($\mathrm{k_x} = 0$).

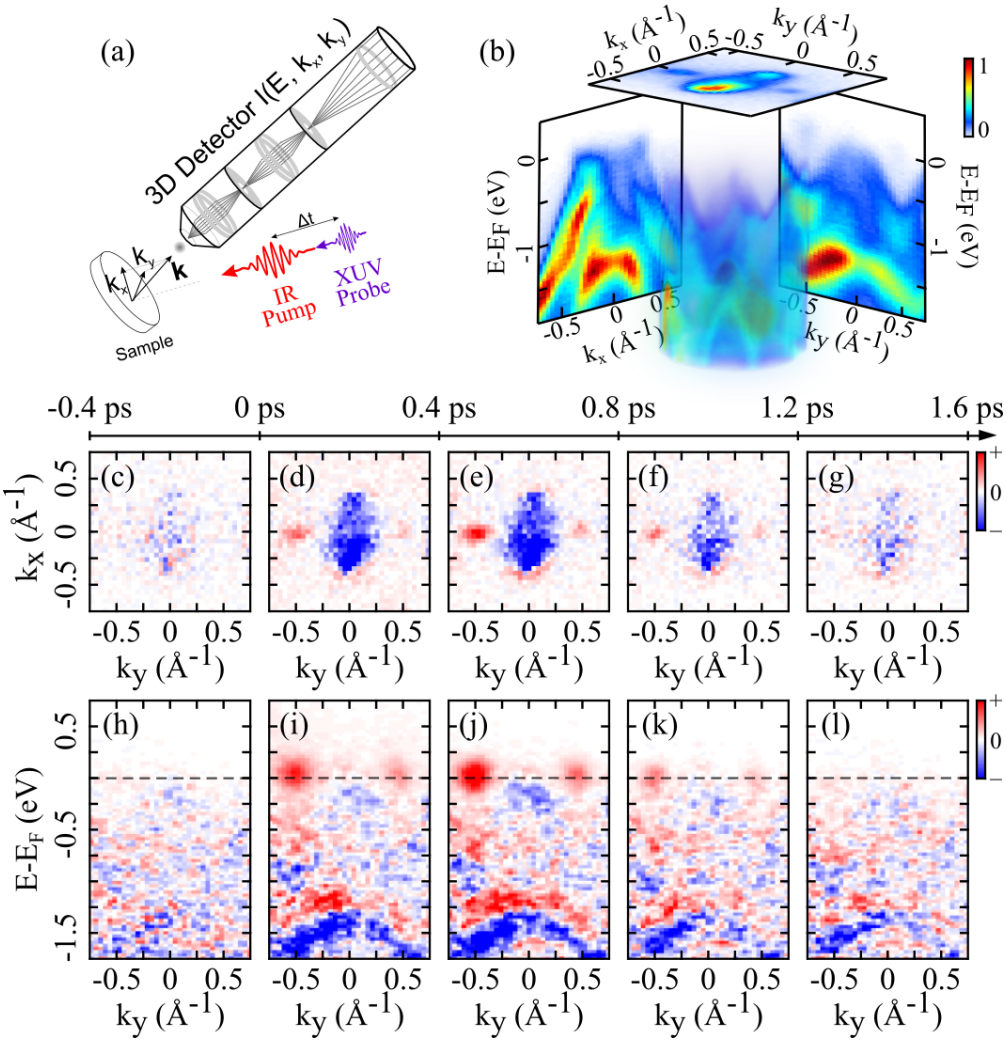

Figure 2: **Ultrafast non-equilibrium Lifshitz transition probed by time-resolved multidimensional photoemission spectroscopy.** (a) A schematic of the experimental setup, featuring IR-pump/XUV-probe pulses and a time-of-flight momentum microscope detector allowing for parallel measurement of the band structure of the crystalline solid, as a function of pump-probe time delay (E_B, k_x, k_y, t). (b) An example of the experimental 3D volumetric photoemission data, as well as cuts along different high-symmetry directions, and cut at the Fermi energy, integrated for all positive time delays. (c)-(g) Differential (unpumped signal subtracted) 2D Fermi surfaces (k_x, k_y) as a function of time delay between the IR pump and the XUV probe. (h)-(l) Corresponding differential energy-resolved cuts along Y-Γ-Y ($k_x = 0$). Each frame represents data integrated for a 400 fs range.

These momentum-energy snapshots reveal the light-induced population dynamics within the γ-pockets accompanied by their time-dependent energy downshift, the latter of which cannot be explained by a transient excited-state population in a rigid band structure picture. Indeed, if the γ-pockets are populated upon photoexcitation, but do not shift downward in energy, the topology of the Fermi surface remains unchanged. Therefore, our data reveal multiple perspectives in witnessing the profound changes taking place at the Fermi surface during the light-driven Lifshitz transition.

What is the microscopic origin of the non-equilibrium modification of the Fermi surface topology? At first glance, two different scenarios can explain the observed ultrafast Lifshitz transition: a light-induced structural phase transition or a light-induced renormalization of the electronic band structure due to dynamical changes in the effective electronic correlations (transient changes of Hubbard U).

As shown in the SI, the γ-pockets lying slightly below the Fermi energy is also a feature of the 1T' phase of $\mathrm{MoTe_2}$. A photoinduced structural phase transition from the $\mathrm{T_d}$ to the 1T' phase would, therefore, lead to the γ-pockets crossing the Fermi level upon photoexcitation, on the timescale of these structural changes. Zhang *et al.* has recently studied this ultrafast lattice symmetry switching ($\mathrm{T_d}$ to 1T') using optical techniques[28]. When pumping above a critical fluence of $>$2 mJ/$\mathrm{cm^2}$, they showed that the structural phase transition occurs on the timescale of $\sim$700 fs and recovers to the $\mathrm{T_d}$ phase within hundreds of picoseconds. Since the pump fluence that we used ($\sim$ 0.6 mJ/$\mathrm{cm^2}$) is significantly lower than the structural phase transition critical fluence, and since

we observe a sub-400 fs modification of the Fermi surface topology with a sub-1.5 ps recovery timescale, the photoinduced structural phase transition can be excluded as a possible explanation of the observed ultrafast Lifshitz transition.

An alternative scenario is that the light-induced Lifshitz transition is of electronic nature and originates from the dynamical modification of U. To investigate the role of the dynamical electronic correlations in the ultrafast Lifshitz transition, we used a self-consistent approach[12] to calculate the time-dependent Hubbard U (TDDFT+U), including a non-thermal distribution of states (dynamical populations) and assuming a frozen lattice. The calculated Fermi surfaces before and after the interaction with the pump pulse, shown in Fig. 3(a)-(b), clearly show that the TDDFT+U simulations predict the light-induced Lifshitz transition.

To gain more insight into the microscopic origin of this topological electronic transition from the simulations, we investigate the ultrafast modification of U upon photoexcitation (Fig. 3(d)-(e)). As predicted for the strongly correlated charge-transfer insulator NiO[13] and a pyrochlore iridate[14], the Hubbard U is found to decrease upon photoexcitation for $\mathrm{T_d}$-$\mathrm{MoTe_2}$. This can be understood in terms of dynamical enhancement of the electronic screening due to the delocalized nature of the pump-induced excited electrons[13].

In the simulations, the modification of the Hubbard U seems to reach a reduced plateau after the end of the laser pulse (Fig. 3 (e)), while in the experiment, the energy of the pockets is delayed compared to the pump laser pulse, timed by the LAPE signal (Fig. 3 (c)). This may be understood as the effect of other processes, such as electron-phonon coupling, unaccounted for

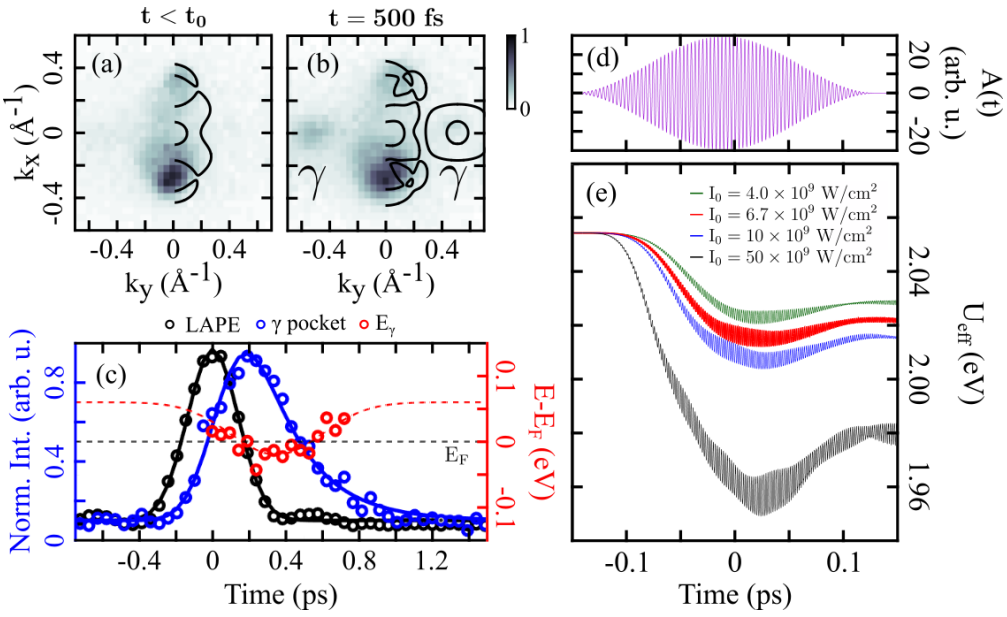

Figure 3: **Ultrafast modification of Hubbard U and the non-equilibrium Lifshitz transition.** (a)-(b) Experimentally measured Fermi surface for $t < t_0$ and t = 500 fs, and Fermi surface before and after the pump pulse, obtained by TDDFT+U simulations using the same fluence as in the experiment (I_0 = 6.7x10^9 W/cm^2). In both cases (theory and experiment), the γ-electron pocket close to the Y point, *i.e.* the hallmark of the Lifshitz transition, is clearly showing up after the interaction with the pump pulse. (c) Normalized laser-assisted photoemission signal (LAPE) (black), the normalized γ-pocket excited-state signal (blue) and energy position of the bottom of the γ-pocket (red), as a function of pump-probe delay. The dashed red curve serves as a guide to the eye. (d) The vector potential of the laser pulse used in the self-consistent TDDFT+U simulations, with the same wavelength and duration as used in the experiment (1030 nm, 140 fs FWHM). (e) Dynamical evolution of U_{eff} for different laser fluences.

in the simulation, that will prevent the laser-driven quenching of U from persisting indefinitely. Moreover, as we reach a non-equilibrium state at the end of the laser pulse, further dynamics is expected to occur before relaxation takes place[14]. Indeed, as one can see in Fig. 3 (c), the γ-pockets first downshifts in energy (in red), transiently crosses the Fermi level (ultrafast Lifshitz transition), and finally shifts back to its original position as the electronic system relaxes to equilibrium via coupling to the lattice.

Moreover, the dynamical reduction of the $\mathrm{U_{eff}}$ (Fig. 3 (e)) is found to be much smaller than what is expected for reaching the Lifshitz transition from equilibrium calculations (Fig. 1 (c)). This can be understood by the fact that, compared to the adiabatic (equilibrium) case, in our non-equilibrium scheme, both dynamical populations and time-dependent Hubbard U can strongly affect the electronic structure and the Fermi surface of $\mathrm{T_d}$-$\mathrm{MoTe_2}$. We, therefore, investigated their respective role in driving the non-equilibrium Lifshitz transition (see SI). From this detailed analysis, we found that modifications of *both* dynamical populations and Hubbard U are required to reach the ultrafast Lifshitz transition. Indeed, for the small dynamical change of $\mathrm{U_{eff}}$ obtained from our time-dependent simulations, no Lifshitz transition would be observed, if the effect of dynamical populations would not be taken into account (adiabatic case). The fact that this novel non-equilibrium route requires a significantly smaller modification of the Hubbard U to reach the Lifshitz transition has strong implications. Indeed, our results establish that the synergy between dynamical populations and Hubbard U can facilitate reaching topological electronic transitions, in cases where only changing U, using adiabatic techniques, would not allow it.

In conclusion, using time-resolved multidimensional photoemission spectroscopy, we have demonstrated a non-equilibrium scheme that allows us to drive an ultrafast Lifshitz transition in the Weyl semimetal T_d-$MoTe_2$. Our *ab initio* simulations revealed that the dominant role of the photoexcitation is the dynamical modulation of the populations and of the electronic correlations, allowing to reach the topological electron transition on ultrafast timescales. In contrary to conventional photoinduced phase transitions, driven by the electronlattice interactions[29], the ultrafast Lifshitz transition presented here is of electronic origin, allowing to switch between different Fermi surface topologies on much faster timescales. Besides the observation of a novel class of Lifshiftz transition, the scheme introduced in our work, based on the ultrafast modification of many-body interactions, is likewise applicable to a wide range of materials. Combining this scheme with the emerging field of twistronics[30] will allow having an unprecedented level of control on the electronic correlations, on timescales not accessible to established adiabatic methods.

Methods

Time-resolved multidimensional photoemission spectroscopy The time-resolved multidimensional photoemission spectroscopy experiments were performed at the Fritz Haber Institute of the Max Planck Society. We used a home-built optical parametric chirped-pulse amplifier (OPCPA) delivering 15 W (800 nm, 30 fs) at 500 kHz repetition rate. The second harmonic of the OPCPA output (400 nm) is used to drive high-order harmonic generation (HHG) by tightly focusing (15 μm FWHM) p-polarized laser pulses onto a thin and dense Argon gas jet. The extremely nonlinear interaction between the laser pulses and the Argon atoms leads to the generation of a comb of odd

harmonics of the driving laser, extending up to the 11th order. The copropagating driving laser and the harmonics are reflected onto a silicon wafer at Brewster's angle of the 400 nm to filter out the energy of the fundamental driving laser. Next, a single harmonic (7th order, 21.7 eV) is isolated by reflection on a focusing multilayer XUV mirror and propagation through a 400 nm thick Sn metallic filter. A photon flux of up to 2x10^{11} photons/s at the sample position is obtained (110 meV FWHM)[27].

As a pump beam, we used a fraction of the compressed 1030 nm pulses used to generate the white-light seed in the OPCPA (pulse duration of $\sim$ 140 fs). The combination of longer wavelength and longer pulse duration (compared with 800 nm, 30 fs, typically used) allows us to use higher pump fluence before reaching the threshold of pump-induced multiphoton photoemission, which introduces space-charge distortion in the time-resolved multidimensional photoemission measurement. Using high-enough fluence is essential to drive the non-equilibrium Lifshitz transition. The drawback is that the temporal resolution decreases to $\sim$ 140 fs FWHM. The pump beam was also linearly p-polarized (along the Γ- X direction of the crystal) and was at an angle of incidence of 65° to the sample surface normal.

The bulk $\mathrm{T_d}$-$\mathrm{MoTe_2}$ samples are cooled to 30 K on the 6-axis cryogenic manipulator (SPECS GmbH) and cleaved at a base pressure of 2x10^{-11} mbar. The data are acquired using a time-of-flight momentum microscope (METIS100, SPECS GmbH), allowing to detect each photoelectron as a single event and as a function of pump-probe delay. The resulting 4D photoemission intensity data have the coordinates I(E_B, k_x, k_y, t).

Concerning the data post-processing, the combination of the high repetition rate of our beamline and the multidimensional data recording scheme[11] leads to typical datasets involving 10^9-10^{11} detected events and a typical dataset size of few hundreds of gigabytes (GBs). We thus use a recently developed open-source workflow[31] to efficiently convert these raw single-event-based datasets into binned calibrated data hypervolumes of the desired dimension, including axes calibration and detector artifact corrections. Binning of the single-event data to a specific hypervolume reduces the data to a manageable size of a few to tens of gigabytes.

DFT+U and TDDFT+U calculations All the calculations presented in the article, as well as in the Supplementary Information (SI), were performed for bulk $\mathrm{T_d}$-$\mathrm{MoTe_2}$, unless stated otherwise. Calculations were performed using fully relativistic Hartwigsen-Goedecker-Hutter (HGH) norm-conserving pseudo-potentials, using the crystal structure taken from[32] (real-space spacing of $\Delta r = 0.158$ Å). Time-dependent calculations have been performed using a $6 \times 5 \times 3$ $\mathbf{k}$-point grid to sample the Brillouin zone, whereas ground-state calculations were performed using a $12 \times 10 \times 6$ $\mathbf{k}$-point grid. We found that this choice does not lead to a sizable change in the value of the computed Hubbard U_{eff}. The pump driving field is taken along the [100] crystallographic direction in all the calculations, which corresponds to the Γ-X direction. We considered a laser pulse of 140 fs duration (FWHM), with a sine-square envelope for the vector potential. The carrier wavelength λ is 1030 nm. The time-dependent wavefunctions and Hubbard U_{eff} are computed by propagating generalized Kohn-Sham equations within real-time TDDFT+U, as provided by the Octopus package[33–35]. We employed the local density approximation for describing the local DFT part, and we computed the effective $U_{\mathrm{eff}} = U - J$ for Mo d orbitals, using localized atomic orbitals from

the corresponding pseudopotentials[12].

We used the real-time TDDFT plus *ab initio* U formalism[12], based on the recently proposed ACBN0 functional [36], which can be seen as a pseudo-hybrid reformulation of the density-functional theory plus Hubbard U (DFT+U) method. The time-dependent generalized Kohn-Sham equation within the adiabatic approximation reads [1]

$$i\frac{\partial}{\partial t}|\psi_{n,\mathbf{k}}(t)\rangle = \Big[\frac{(\hat{\mathbf{p}}-\mathbf{A}(t)/c)}{2} + \hat{v}_{\rm ext} + \hat{v}_{\rm H}[n(\mathbf{r},t)] + \hat{v}_{\rm xc}[n(\mathbf{r},t)] + \hat{V}_U[n(\mathbf{r},t),\{n^{\sigma\sigma'}_{mm'}\}]\Big]|\psi_{n,\mathbf{k}}(t)\rangle, \quad (1)$$

where $|\psi_{n,\mathbf{k}}\rangle$ is a Pauli spinor representing the Bloch state with a band index n, at the point $\mathbf{k}$ in the Brillouin zone, $\hat{v}_{\rm ext}$ is the ionic potential, $\mathbf{A}(t)$ is the external vector potential describing the laser field, $\hat{v}_{\rm H}$ is the Hartree potential, $\hat{v}_{\rm xc}$ is the exchange-correlation potential, and $\hat{V}^{\sigma}_{U}$ is the (non-local) operator,

$$\hat{V}_U[n,\{n^{\sigma\sigma'}_{mm'}\}] = U_{\rm eff}\sum_{m,m'}(\frac{1}{2}\delta_{mm'} - n_{mm'})\hat{P}_{m,m'}\,. \quad (2)$$

Here $\hat{P}^{\sigma\sigma'}_{mm'} = |\phi^{\sigma}_{m}\rangle\langle\phi^{\sigma'}_{m'}|$ is the projector onto the localized subspace defined by the localized orbitals $\{\phi^{\sigma}_{m}\}$, and $n^{\sigma\sigma'}$ is the density matrix of the localized subspace, both of these quantity been non-diagonal is spin space[12]. The expressions of U and J can be found for instance in Ref.[12] for the non-collinear spin case.

[1]The nonlocal part of the pseudopotential is omitted for conciseness.

Acknowledgements This work was funded by the Max Planck Society, the European Research Council (ERC) under the European Unions Horizon 2020 research and innovation program (Grant No. ERC-2015-CoG-682843 and ERC-2015-AdG694097), the German Research Foundation (DFG) within the Emmy Noether program (Grant No. RE 3977/1 and MS 2558/2-1), the Cluster of Excellence "Advanced Imaging of Matter" (AIM), Grupos Consolidados (IT1249-19), the SFB925 "Light induced dynamics and control of correlated quantum systems" and the Collaborative Research Center/Transregio 227 "Ultrafast Spin Dynamics" (project B07). The Flatiron Institute is a division of the Simons Foundation. S.B. acknowledges financial support from the NSERC-Banting Postdoctoral Fellowships Program.

Author contributions S.B., S.D., M.D., J.M., T.P. and L.R. performed the time-resolved multidimensional photoemission spectroscopy experiments. S.B. analyzed the experimental data. R.P.X developed the open source workflow for data preprocessing. R.E., L.R. and M.W. were responsible for developing the infrastructures allowing these measurements as well as for the overall project direction. N.T.D. performed the theoretical calculations, their analysis and interpretation, with the guidance of M.A.S. and A.R. S.B. wrote the first draft with inputs from N.T.D., M.A.S., and R.E. All authors contributed to the discussions and the final version of the manuscript.

Competing Interests The authors declare that they have no competing financial interests.

Correspondence Correspondence and requests for materials should be addressed to S.B. (beaulieu@fhi-berlin.mpg.de), N.T.D. (nicolas.tancogne-dejean@mpsd.mpg.de) or R.E. (ernstorfer@fhi-berlin.mpg.de).

Supplementary information

I. Additional experimental data

Dynamics along X-Γ-X

In Fig. 2 of the main paper, we presented differential Fermi surfaces and cuts along Y-Γ-Y ($\mathrm{k_x} = 0$) direction, to show the unambiguous signature of Lifshitz transition. Our multidimensional detection scheme allows us to measure differential signals along any direction of the Brillouin zone with sufficient counting statistics. To compare our data with previously published time- and angle-resolved photoemission spectroscopy (ARPES) results on the same material, we can plot the photoemission differential signal along X-Γ-X ($\mathrm{k_y} = 0$) high-symmetry direction, as reported by Crepaldi *et al.* [37]. The strong enhancement of the signal around $\pm$ 0.25 $\mathrm{\AA}^{-1}$ above the Fermi level, the depletion around Γ below the Fermi level, as well as the extracted excited states lifetime of $\sim$ 270 fs, from our experimental data presented on Fig. 4, is in good agreement with the observations of Crepaldi *et al.*, who studied the enhanced ultrafast relaxation rate in the Weyl semimetallic (low temperature) phase of $\mathrm{MoTe_2}$. In that paper, the authors didn't report the dynamics along Γ-Y, which is the direction along which the signature of the Lifshitz transition is the most evident.

Time-dependent electronic temperature

We have extracted the time-dependent electronic temperature, to estimate the heating of the electronic system by the pump pulse. This information provides a reference point for theoretical simulations, presented in the next sections. To do so, we fitted the momentum-integrated energy

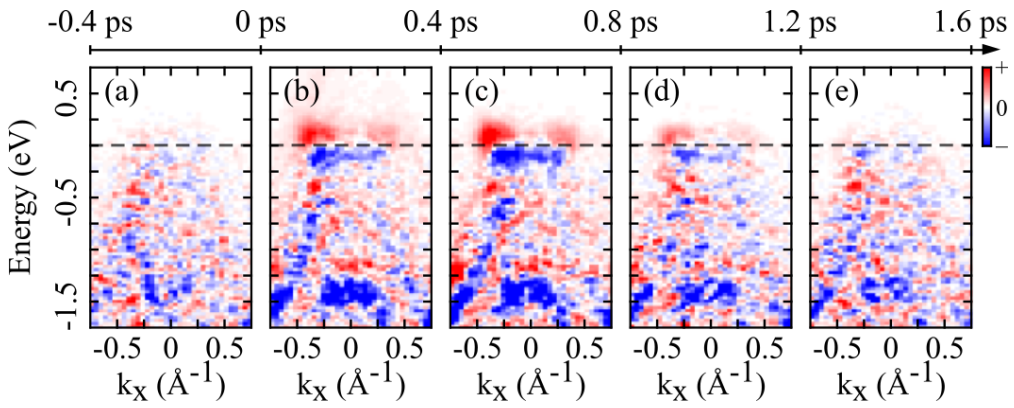

Figure 4: **Ultrafast electronic dynamic along X-Γ-X.** (a)-(e) Differential (signal before time-zero subtracted) energy-resolved cuts along X-Γ-X ($k_y = 0$) as a function of time delay between the IR pump and the XUV probe. These data are extracted from the same scan as for Fig. 2 of the main text. The pump pulse intensity is estimated to be 6.7x10^9 W/cm^2.

spectra measured experimentally by Fermi-Dirac distribution functions convolved with a Gaussian function as the spectral instrument response function. First, we have fixed the electronic temperature of the Fermi-Dirac distribution to 30 K and kept the Gaussian width as a free parameter of the fit, for the case of the unpumped system, to estimate the instrument response function. Next, we have fixed the instrument response function (the Gaussian width), and fit a Fermi-Dirac distribution for each pump-probe delays, keeping the electronic temperature as a free parameter of the fit. The results of the fit are shown in Fig. 5.

As shown in Fig. 5, after the interaction with the pump laser pulse, the electronic temperature increases to almost 600 K and then gradually recovers to the original temperature of $\sim$ 30 K, within a time-scale similar to the excited states population lifetime (signal above the Fermi level). As explained in the theoretical section of the Supplementary Information, this increase of

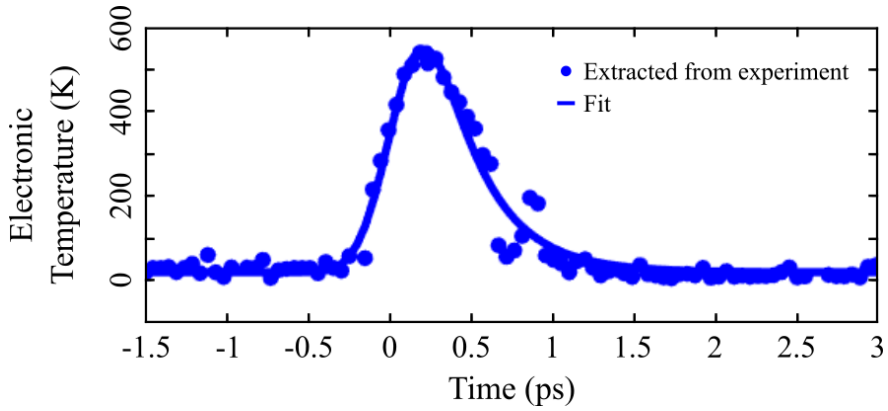

Figure 5: **Time-dependent electronic temperature.**: Electronic temperature as a function of pump-probe delay, extracted from fitting the momentum-integrated energy spectra by a resolution-broadened Fermi-Dirac distribution function.

the electronic temperature (dynamical populations), combined with the dynamical modification of Hubbard U_{eff}, is at the origin of the ultrafast non-equilibrium Lifshitz transition.

II. Adiabatic Lifshitz transition

We first theoretically analyze the adiabatic Lifshitz transition and in particular the effect of U_{eff} on the energy position of the γ-pocket. For this, we performed a set of DFT+U calculations while varying U_{eff}. Our results are shown in Fig. 1c in the main text. The self-consistently evaluated U_{eff} is found to be 2.05 eV. From our calculations, we find that the Lifshitz transition occurs around 1.5 eV, which is consistent with the value obtained from a similar analysis by Xu *et al.* [19].

From these data, we find that in the adiabatic limit, for a 70 meV change in position of the γ-pocket, which has been measured experimentally, (see Fig. 3c in the main text), a change in

U_{eff} of 1.8 eV is required. This is in clear contrast with the results obtained in Fig. 3e from our TDDFT+U calculations, from which the change in U_{eff} at the experimental intensity is estimated to be around 30 meV only. Thus, our results indicate that the measured energy downshifts of the pocket, ultimately leading to the Lifshitz transition, cannot originate only from an adiabatic change of U_{eff} and that more subtle dynamics are at play here.

Note that we carefully checked that the laser-induced changes in U_{eff} are converged and that adding more $\mathbf{k}$-point to sample the Brillouin zone do not lead to sizable differences in the dynamics of U_{eff}. Moreover, note that due to numerical artifacts, the Fig. 3a and Fig. 3b are obtained without spin-orbit coupling included. Whereas the main results are not affected by the inclusion or not of the spin-orbit coupling, the Wannierization procedure, employed to get the Fermi surface cut from the non-equilibrium states, is found to be less stable when the spin-orbit coupling is included.

We want to point out the analogy to the creation of a Weyl semimetallic phase induced by a laser in pyrochlore iridates, that some of us predicted [14]. Indeed, in this previous work, we showed that light-induced reduction of U_{eff} is leading to the transient appearance of a Weyl semimetallic phase in pyrochlore irridate for values of U_{eff} for which, according to the equilibrium (adiabatic) phase diagram, should not allow it.

The experimentally measured change in the pocket position also shows a clear delay between the change in the pocket energy position and the laser pulse itself (timed by the LAPE signal, Fig. 3b in the main text), indicating that some transient dynamics still takes place after the end of the laser pulse and before the material starts to returns to its ground state due to thermalization

effects. This is an indication that the system is brought to a non-equilibrium state at the end of the laser pulse.

As discussed below, our results provide evidence explaining the observed light-induced Lifshitz transition, but we found that one needs to take into account the non-equilibrium dynamics induced by the laser and not only a simpler adiabatic change of the Hubbard U_{eff}.

III. Non-equilibrium Fermi surface

From the theoretical point of view, the Fermi surface is a concept that is well defined at equilibrium, and for a vanishing temperature. However, in time- and angle-resolved photoemission experiments, it is possible to measure the Fermi surface evolving in time for a fixed Fermi energy, taking as reference the equilibrium value. Here, we aim at comparing this measured non-equilibrium Fermi surface to the results of our time-dependent simulations, which include both the change in populations and time-evolved Hubbard U. We employed for this the non-equilibrium states taken after the end of the laser pulse and computed the corresponding energies

$$E^{\mathrm{neq}}_{n\mathbf{k}}(t) = \langle \psi_{n\mathbf{k}}(t) | \hat{H}(t) | \psi_{n\mathbf{k}}(t) \rangle, \tag{3}$$

where n refers to a band index, $\mathbf{k}$ is the $\mathbf{k}$-point index, $\psi_{n\mathbf{k}}(t)$ the Pauli spinor representing the Bloch state obtained from the time-evolution of the TDDFT Kohn-Sham equations, and $\hat{H}[n(t)](t)$ is the Hamiltonian constructed from the time-evolved electronic density $n(t)$ as well as $U_{\mathrm{eff}}(t)$ and the corresponding non-equilibrium occupations $n^{\sigma\sigma'}_{mm'}(t)$.

We note that using these energies after the end of the laser pulse (*i.e.* when there is no vector potential due to the laser) makes the result of our analysis gauge invariant. Alternatively, one might want to use the adiabatic eigenvalues, $E^{ad}_{n\mathbf{k}}(t)$, of the time-evolved Hamiltonian, $\hat{H}(t)$, to investigate the non-equilibrium Fermi surface defined by

$$\hat{H}(t)|\psi^{\mathrm{ad}}_{n\mathbf{k}}\rangle = E^{\mathrm{ad}}_{n\mathbf{k}}(t)|\psi^{\mathrm{ad}}_{n\mathbf{k}}\rangle. \tag{4}$$

Here, similar to the previous case, $\hat{H}(t)$ is the Hamiltonian constructed from the time-evolved electronic density $n(t)$ as well as $U_{\mathrm{eff}}(t)$ and the corresponding non-equilibrium occupations $n^{\sigma\sigma'}_{mm'}(t)$.

We found that the adiabatic states do not show any Lifshitz transition compared to the non-equilibrium states, which is fully consistent with our analysis above. Indeed, if the adiabatic states would show a Lifshitz transition, the band structure corresponding to the Hamiltonian constructed from $U(t)$ would show a Lifshitz transition, which we have shown not to be the case for the excitation density used in this experiment. This is a strong indication of the non-adiabatic nature of the measured Lifshitz transition.

IV. Effect of dynamical U

We further analyze the role of the different ingredients to reach the Lifshitz transition. From the theoretical results presented in the main text, the change of U_{eff} is found to be quite small in Fig. 3e, compared to what could be expected from the equilibrium phase diagram (Fig. 1c in the main text), in order to reach the Lifshitz transition. To disentangle the different effects taking place, we also performed a time-dependent simulation with a frozen U_{eff} and compared with the result

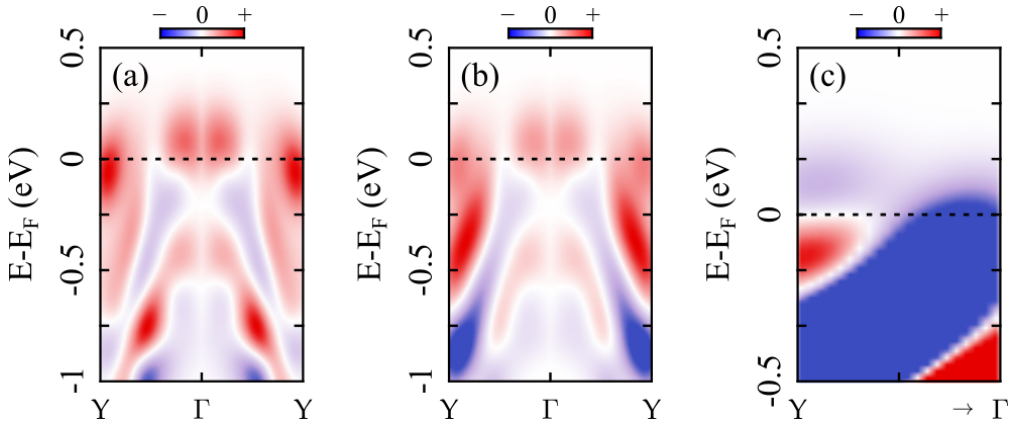

Figure 6: **Effect of dynamical U_{eff} along Y-Γ-Y.** a) Calculation performed from the excited states obtained at the end of the laser pulse for a dynamical U_{eff} calculation. b) Same as a) but for a frozen U_{eff} calculation. c) Difference of the two signals, *i.e.* (a) and (b), close to the position of the pocket.

with a time-evolving U_{eff} presented in the main text. This analysis allows us to clearly identify the role of dynamical U_{eff} in driving the Lifshitz transition. Indeed, for a time-dependent U_{eff}-frozen simulation, the non-adiabatic nature of the time-evolved states is still taken into account, as well as dynamical populations, as described by the local-density approximation, but the dynamical correlations (captured by time-evolving U_{eff}) are not included.

For a clearer comparison with the experimental results, we simulate an angle-resolved photoemission signal from the excited-state eigenvalues. We employed Wannier90 [38] to interpolate the band structures on a finer **k**-point grid. We, then, convoluted in energy and in momentum by a Gaussian whose widths correspond to the experimental resolutions, respectively 120 meV and 0.05Å^{-1}.

Our results are shown in Fig. 6 for the Y-Γ-Y direction, *i.e.* the direction where the hallmark

of the Lifshitz transition, and we found that γ-pocket crossing the Fermi level, appears. From these data, it is clear that the appearance of the γ-pocket in the angle-resolved photoemission signal crucially depends on the dynamical $U_{\rm eff}$. Indeed, in Fig. 6(b), the signal of the pocket does not appear clearly, whereas it is the dominating feature in Fig. 6(a). As evidenced by the difference close to the position of the γ-pocket, which displays a clear differential profile, the dynamical $U_{\rm eff}$ calculation yields a pocket below the Fermi energy whereas the frozen $U_{\rm eff}$ approach yields a pocket at higher energy. This is a clear indication that the dynamical correlations are a crucial ingredient to observe the Lifshitz transition.

We also computed similar plots for the X-Γ-X direction (see Fig. 7) for which $U_{\rm eff}$ is expected not to play an important role. As expected, we do not observe any qualitative difference between the frozen and dynamical $U_{\rm eff}$ calculations, confirming the validity of our approach.

Importantly, in both cases, we note that the simulated ARPES spectra are qualitative agreement with the experimental ARPES signals (see Fig. 2 in the main text and Fig. 4). Finally, we note that these results employ here a crude approximation to the measured ARPES signal, in which transition dipole matrix elements are not taken into account, which would correspond to more intricate and numerically more expensive TDDFT calculations in supercell [39].

V. Note on the role of dynamical populations

As shown in the main text, the full TDDFT+$U_{\rm eff}$ simulations, which include both the dynamical evolution of $U_{\rm eff}$ and of the populations, predict the ultrafast Lifshitz transition. Moreover, the

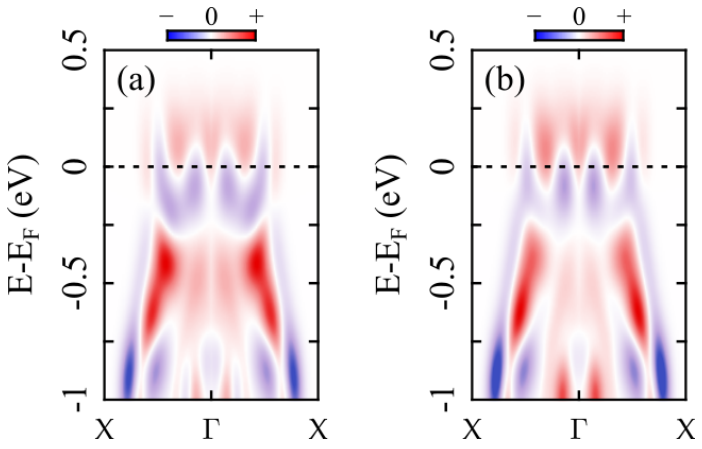

Figure 7: **Effect of dynamical U_{eff} along X-Γ-X.** a) Calculation performed from the excited states obtained at the end of the laser pulse for a dynamical U_{eff} calculation. b) Same as a) but for a frozen U_{eff} calculation.

comparison between the non-equilibrium simulations performed with frozen and with dynamical U_{eff} (Fig. 6) showed that even if Hubbard U_{eff} do not reach the adiabatic critical value ($U_{\text{eff}} \sim$ 1.5 eV) to reach the Lifshitz transition, the inclusion of dynamical U_{eff} is essential to reach the non-equilibrium Lifshitz transition. By taking into account these observations, we argue that both the dynamical modification of the U_{eff}, and of the populations, are necessary to reach the ultra-fast non-equilibrium Lifshitz transition. This also implies that the novel non-equilibrium route requires a significantly smaller change in the Hubbard U_{eff} than the adiabatic case to reach the Lifshitz transition.

VI. Band structure of $1\text{T}'$-MoTe_2

We also performed simulations for the $1\text{T}'$-phase of MoTe_2 (see Fig. 8), which is the high temperature phase. We employed the same parameters as for equilibrium studies of T_d-MoTe_2,

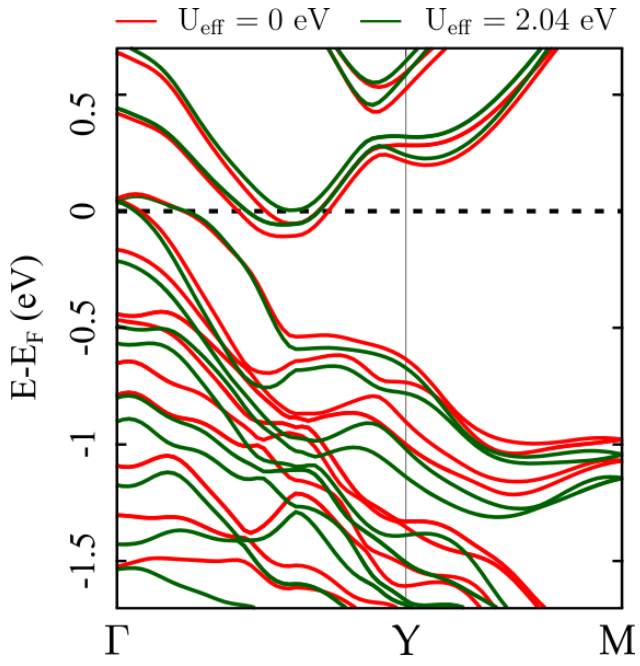

Figure 8: **Band structure of** $1\mathrm{T}'$**-**$\mathrm{MoTe_2}$. The electronic band structure of $1\mathrm{T}'$-$\mathrm{MoTe_2}$ for the equilibrium self-consistent value of U_{eff} = 2.04 eV (in green) and for the reduced value of U_{eff} = 0 eV.

and used the previously reported atomic coordinates [32]. We performed both DFT and DFT+U calculations, in which we evaluated the *ab initio* U_{eff}, see Sec. III for more details. As an important result, we found that even including a Hubbard U_{eff} of 2.04 eV (obtained from first principles), the γ-pocket of the $1\mathrm{T}'$ phase of $\mathrm{MoTe_2}$ is located below the Fermi energy.

This shows that at equilibrium, the $1\mathrm{T}'$- and the $\mathrm{T_d}$-phase have different Fermi surface topologies. This raises the question of whether the measured data corresponds to a light-induced structural phase transition to the high-temperature $1\mathrm{T}'$ phase, as observed in Ref. [28]. We argue in detail in the main text that this is not the case. Briefly, the pump fluence that we used ($\sim$ 0.6 mJ/$\mathrm{cm^2}$) is significantly lower than the structural phase transition critical fluence ($>$2 mJ/$\mathrm{cm^2}$), and the timescales relevant for the experimentally observed Lifshitz transition are completely different than the

ones associated with the light-induced structural phase transition [28].

1. Kaganov, M. I. & Lifshitz, I. M. Electron theory of metals and geometry. *Phys. Usp.* **22**, 904–927 (1979).

2. Lifshitz, I. M. Anomalies of electron characteristics of a metal in the high pressure region. *Journal of Experimental and Theoretical Physics* **38**, 1569 (1960).

3. Xiang, Z. J. *et al.* Pressure-induced electronic transition in black phosphorus. *Phys. Rev. Lett.* **115**, 186403 (2015).

4. Liu, C. *et al.* Evidence for a Lifshitz transition in electron-doped iron arsenic superconductors at the onset of superconductivity. *Nature Physics* **6**, 419–423 (2010).

5. Shi, X. *et al.* Enhanced superconductivity accompanying a Lifshitz transition in electron-doped FeSe monolayer. *Nature Communications* **8**, 14988 (2017).

6. Sunko, V. *et al.* Direct observation of a uniaxial stress-driven Lifshitz transition in $\mathrm{Sr_2RuO_4}$. *npj Quantum Materials* **4**, 46 (2019).

7. Burganov, B. *et al.* Strain control of Fermiology and many-body interactions in two-dimensional ruthenates. *Phys. Rev. Lett.* **116**, 197003 (2016).

8. Kang, D. *et al.* Superconductivity emerging from a suppressed large magnetoresistant state in tungsten ditelluride. *Nature Communications* **6**, 7804 (2015).

9. Wu, Y. *et al.* Temperature-induced Lifshitz transition in $\mathrm{WTe_2}$. *Phys. Rev. Lett.* **115**, 166602 (2015).

10. Zhang, Y. *et al.* Electronic evidence of temperature-induced Lifshitz transition and topological nature in $\mathrm{ZrTe_5}$. *Nature Communications* **8**, 15512 (2017).

11. Kutnyakhov, D. *et al.* Time- and momentum-resolved photoemission studies using time-of-flight momentum microscopy at a free-electron laser. *Review of Scientific Instruments* **91**, 013109 (2020).

12. Tancogne-Dejean, N., Oliveira, M. J. T. & Rubio, A. Self-consistent $\mathrm{DFT} + U$ method for real-space time-dependent density functional theory calculations. *Phys. Rev. B* **96**, 245133 (2017).

13. Tancogne-Dejean, N., Sentef, M. A. & Rubio, A. Ultrafast modification of Hubbard U in a strongly correlated material: Ab initio high-harmonic generation in NiO. *Phys. Rev. Lett.* **121**, 097402 (2018).

14. Topp, G. E., Tancogne-Dejean, N., Kemper, A. F., Rubio, A. & Sentef, M. A. All-optical nonequilibrium pathway to stabilising magnetic Weyl semimetals in pyrochlore iridates. *Nature Communications* **9**, 4452 (2018).

15. Sun, Y., Wu, S.-C., Ali, M. N., Felser, C. & Yan, B. Prediction of Weyl semimetal in orthorhombic $\mathrm{MoTe_2}$. *Phys. Rev. B* **92**, 161107 (2015).

16. Deng, K. *et al.* Experimental observation of topological Fermi arcs in type-II Weyl semimetal $\mathrm{MoTe_2}$. *Nature Physics* **12**, 1105–1110 (2016).

17. Huang, L. *et al.* Spectroscopic evidence for a type-II Weyl semimetallic state in $MoTe_2$. *Nature Materials* **15**, 1155–1160 (2016).

18. Tamai, A. *et al.* Fermi arcs and their topological character in the candidate type-II Weyl semimetal $MoTe_2$. *Phys. Rev. X* **6**, 031021 (2016).

19. Xu, N. *et al.* Evidence of a Coulomb-interaction-induced Lifshitz transition and robust hybrid Weyl semimetal in $MoTe_2$. *Phys. Rev. Lett.* **121**, 136401 (2018).

20. Medjanik, K. *et al.* Direct 3D mapping of the Fermi surface and Fermi velocity. *Nature Materials* **16**, 615–621 (2017).

21. Zhou, Q. *et al.* Hall effect within the colossal magnetoresistive semimetallic state of $\mathbf{MoTe_2}$. *Phys. Rev. B* **94**, 121101 (2016).

22. Soluyanov, A. A. *et al.* Type-II Weyl semimetals. *Nature* **527**, 495–498 (2015).

23. Wan, X., Turner, A. M., Vishwanath, A. & Savrasov, S. Y. Topological semimetal and Fermi-arc surface states in the electronic structure of pyrochlore iridates. *Phys. Rev. B* **83**, 205101 (2011).

24. Xu, S.-Y. *et al.* Discovery of a Weyl Fermion semimetal and topological Fermi arcs. *Science* **349**, 613–617 (2015).

25. Hosur, P. & Qi, X. Recent developments in transport phenomena in Weyl semimetals. *Comptes Rendus Physique* **14**, 857 – 870 (2013).

26. Aryal, N. & Manousakis, E. Importance of electron correlations in understanding photoelectron spectroscopy and Weyl character of $MoTe_2$. *Phys. Rev. B* **99**, 035123 (2019).

27. Puppin, M. *et al.* Time- and angle-resolved photoemission spectroscopy of solids in the extreme ultraviolet at 500 kHz repetition rate. *Review of Scientific Instruments* **90**, 023104 (2019).

28. Zhang, M. Y. *et al.* Light-induced subpicosecond lattice symmetry switch in $MoTe_2$. *Phys. Rev. X* **9**, 021036 (2019).

29. Nicholson, C. W. *et al.* Beyond the molecular movie: Dynamics of bands and bonds during a photoinduced phase transition. *Science* **362**, 821–825 (2018).

30. Yankowitz, M. *et al.* Tuning superconductivity in twisted bilayer graphene. *Science* **363**, 1059–1064 (2019).

31. Xian, R. P. *et al.* An open-source, distributed workflow for band mapping data in multidimensional photoemission spectroscopy *[arXiv:1909.07714]* (2019).

32. Qi, Y. *et al.* Superconductivity in Weyl semimetal candidate $MoTe_2$. *Nature Communications* **7**, 11038 (2016).

33. Tancogne-Dejean, N. *et al.* Octopus, a computational framework for exploring light-driven phenomena and quantum dynamics in extended and finite systems *[arXiv:1912.07921]* (2019).

34. Andrade, X. *et al.* Real-space grids and the octopus code as tools for the development of new simulation approaches for electronic systems. *Phys. Chem. Chem. Phys.* **17**, 31371–31396 (2015).

35. Castro, A. *et al.* Octopus: a tool for the application of time-dependent density functional theory. *Physica Status Solidi B* **243**, 2465–2488 (2006).

36. Agapito, L. A., Curtarolo, S. & Buongiorno Nardelli, M. Reformulation of $\mathrm{DFT} + U$ as a pseudohybrid Hubbard density functional for accelerated materials discovery. *Phys. Rev. X* **5**, 011006 (2015).

37. Crepaldi, A. *et al.* Enhanced ultrafast relaxation rate in the Weyl semimetal phase of $\mathrm{MoTe_2}$ measured by time- and angle-resolved photoelectron spectroscopy. *Phys. Rev. B* **96**, 241408 (2017).

38. Pizzi, G. *et al.* Wannier90 as a community code: new features and applications. *Journal of Physics: Condensed Matter* **32**, 165902 (2020).

39. De Giovannini, U., Huebener, H. & Rubio, A. A first-principles time-dependent density functional theory framework for spin and time-resolved angular-resolved photoelectron spectroscopy in periodic systems. *Journal of Chemical Theory and Computation* **13**, 265–273 (2016).